Brittle to ductile transition during compression of glassy nanoparticles studied in molecular dynamics simulations *⊗*

Marx Akl (i); Liping Huang (i); Yunfeng Shi ■ (ii)



J. Appl. Phys. 134, 035104 (2023) https://doi.org/10.1063/5.0151127





CrossMark

Articles You May Be Interested In

Porosity and the brittle-ductile transition in sedimentary rocks

AIP Conference Proceedings (March 1987)

Spontaneous brittle-to-ductile transition in aqueous foam

Journal of Rheology (May 2012)

Ductile to brittle transition in dynamic fracture of brittle bulk metallic glass

J. Appl. Phys. (May 2008)

500 kHz or 8.5 GHz? And all the ranges in between.









Brittle to ductile transition during compression of glassy nanoparticles studied in molecular dynamics simulations

Cite as: J. Appl. Phys. 134, 035104 (2023); doi: 10.1063/5.0151127 Submitted: 18 March 2023 · Accepted: 17 June 2023 · Published Online: 21 July 2023







Marx Akl, 1,2 Liping Huang, 2 and Yunfeng Shi^{2,a)}

AFFILIATIONS

- Department of Physics, Applied Physics, and Astronomy, Rensselaer Polytechnic Institute, 110 8th St., Troy, New York 12309, USA
- ²Department of Materials Science and Engineering, Rensselaer Polytechnic Institute, 110 8th St., Troy, New York 12309, USA

ABSTRACT

Understanding how nanoparticles deform under compression not only is of scientific importance but also has practical significance in various applications such as tribology, nanoparticle-based probes, and the dry grinding of raw materials. In this study, we conducted compression tests on model brittle glassy nanoparticles using molecular dynamics simulations. We found that during the early stages of plastic $\frac{\aleph}{2}$ deformation, shear bands formed in a similar pattern regardless of the nanoparticle size. However, as the deformation continued, dominant examples of the nanoparticles while being suppressed in smaller ones. This size-dependent brittle-to-ductile transition can be explained by a simple model beside on Griffith's theory. We also investigated the effect of the surface stress state on fracture using the smaller. explained by a simple model based on Griffith's theory. We also investigated the effect of the surface stress state on fracture using thermally tempered nanoparticles. We observed that the presence of compressive surface stress strengthened the nanoparticle by suppressing crack formation, even when a pre-notch was present. On the other hand, tensile surface stress had the opposite effect. Interestingly, nanoparticles with both tensile and compressive surface stress promoted shear deformation, which could potentially compromise the mechanical performance of tempered glass despite delayed crack formation.

Published under an exclusive license by AIP Publishing. https://doi.org/10.1063/5.0151127

I. INTRODUCTION

Mechanical properties of nanoparticles are of fundamental importance in many fields of science and engineering. The elasticity, plasticity, and fracture of a single nanoparticle, particularly the size dependence, are not only interesting mechanical problems of materials, but also crucial in engineering applications in which nanoparticles are under mechanical loading. Understanding the deformation of third body particulates between moving contacts, such as solid lubricants and wear debris, constitutes one of the grand challenges in tribology. Single-nanoparticle-terminated tips have been developed for scanning probe microscopy,2 the operating condition and device reliability³ of which demand a quantitative understanding of the deformation behavior of single nanoparticles. Mechanical milling is a cost-effective way of nanoparticle synthesis directly from bulk materials, 4 yet its efficacy relies on the fracture of brittle particles, which becomes harder as the size reduces.5 Furthermore, the knowledge of how a single nanoparticle deforms

under compression is foundational to the comprehend deformation of nanogranular materials⁶ in which nanoparticles compress/shear/ adhere against one another. For instance, the room-temperature impact consolidation method, 7,8 universally applicable among brittle aerosol particles, relies on the brittle-to-ductile (BTD) transition as the aerosol particle becomes smaller.

There are a wide range of nanomechanical tests to characterize the mechanical properties of nanomaterials of different shapes and sizes. 9-12 Uniaxial tension tests have been carried out on nanowires, nanopillars, and focused-ion-beam-carved miniaturized dog-bone samples. In addition, uniaxial compression tests have been conducted on nanopillar samples. 13-15 However, there are only a few experimental reports on the compression of nanowires and nanoparticles. The compression test on a glassy silica particle 16 about half a micrometer in diameter has been conducted in a transmission electron microscope, in which silica glass plastically flows facilitated by a high intensity electron beam. Similar in situ nanoparticle compression has been reported on platinum, 17 diesel soot nanoparticles, 18 alumina, 1

a) Author to whom correspondence should be addressed: shiy2@rpi.edu

and nickel-iron alloys.20 A recently developed technique termed laser induced particle impact test (LIPIT)^{21–23} is capable of launching spherical microparticles onto targets with km/s speed, causing damage to both the microparticle and the target. The LIPIT could be viewed as the impact nanocompression test of spherical particles, given that the particles are much softer than the target.

The molecular dynamics (MD) simulation method has played an increasingly important role in the field of nanomechanics, including the modeling of nanoparticle deformation.²⁴ The elastic behavior of carved single crystal platinum nanoparticles with different shapes and facets has been simulated under compression, which exhibits surface-induced size-dependent modulus, 25 as well as the emission of partial dislocations and the formation of stacking faults during plastic flow.¹⁷ MD simulation has also been used to model the compression of diesel soot nanoparticles with different combinations of carbon hybridization states. 18,26 Phase transformation from diamond cubic to beta-tin has been seen in the compression of silicon nanoparticles around 10 nm in radius, which can be partially reversed upon annealing at higher temperature.²⁷ Another MD simulation of silicon nanoparticles under compression showed that the notion of "smaller is strong" is shape-dependent. 28 Faceted metallic nickel-iron nanoparticles have also been simulated in which dislocation nucleation depends sensitively on solute distribution.2

The key questions on the mechanical behavior of nanoparticles are on the size-dependent yield strength, fracture strength, or phase transition threshold. Based on Griffith's energy argument that the stored elastic energy drives the formation of new crack surfaces, Kendall⁵ showed that the fracture strength under compression of a brittle particle increases as its size reduces. By considering a specific particle shape (rectangular plate sharped on one end), Kendall developed a critical BTD particle size, below which the particles are ductile. In fact, such BTD energy argument can be generalized for yield and phase transition by balancing the stored elastic energy with the energy cost for the deformed/transformed region. In the present work, we focused on understanding the BTD transition of nanoparticles under compression. Glassy nanoparticles were chosen here to avoid the complexity associated with anisotropy and facets of crystalline nanoparticles. Furthermore, the elasticity of a spherical isotropic nanoparticle can be well described by the Hertzian contact theory, reciprocating indentation with a spherical indenter. In addition to understanding the BTD transition for brittle nanoparticles, we also aim at examining how different strain gradients affect the mechanical behavior of nanoparticles. This is partly motivated by many existing sample preparation imposing surface strain gradients with the purpose of enhancing mechanical performance such as chemical tempering, 29 thermal tempering,³⁰ and surface mechanical attrition treatment.³

II. SIMULATION METHODOLOGY

A. Interatomic potential

Molecular dynamics (MD) simulations were conducted using the LAMMPS package³³ to study an equimolar binary glass forming system modeled by a modified Lennard-Jones potential.³ This pairwise potential features an energy penalty in the form of

that the fracture strength under compresincreases as its size reduces. By considering that the fracture strength under compressincreases as its size reduces. By considering the form of bump (analogous to an energy barrier) to tune the ductility of the resulting model glass,

$$\varphi_{mBLJ}(r) = \begin{cases}
4\varepsilon_{\alpha\beta} \left(\frac{\sigma_{\alpha\beta}^{12}}{r^{12}} - \frac{\sigma_{\alpha\beta}^{6}}{r^{6}} \right) - \varepsilon_{cutoff}, & r < r_{\alpha\beta}^{s}, \\
4\varepsilon_{\alpha\beta} \left(\frac{\sigma_{\alpha\beta}^{12}}{r^{12}} - \frac{\sigma_{\alpha\beta}^{6}}{r^{6}} \right) - \varepsilon_{cutoff} + \varepsilon_{B}\varepsilon_{LL}\sin^{2}\left(\pi \frac{r_{\alpha\beta}^{c} - r}{r_{\alpha\beta}^{c}} - r_{\alpha\beta}^{s}\right), & r_{\alpha\beta}^{c} > r \ge r_{\alpha\beta}^{s}, \\
0, & r \ge r_{\alpha\beta}^{c},
\end{cases}$$
(1)

where $arepsilon_{lphaeta}$ and $\sigma_{lphaeta}$ denote the energy and length scales of the equimolar glass forming mixture, respectively. The two types of atoms, denoted by L and S, have different masses: $m_L = 2m_0$, $m_S = m_0$. All bonds in the mixture share the same strength: $\varepsilon_{LL} = \varepsilon_{LS} = \varepsilon_{SS}$; however, the bond length is set as $\sigma_{SS} = \frac{5}{6}\sigma_{LL}$ and $\sigma_{LS} = \frac{11}{12}\sigma_{LL}$. The cutoff $r_{\alpha\beta}^c$ is chosen to be species dependent, $r_{LL}^c = 1.4\sigma_{LL}, r_{LS}^c = 1.2833\sigma_{LL}, r_{SS}^c = 1.1667\sigma_{LL}$. Thus, only the first nearest neighbor atoms are interacting with each other. The energy penalty is superimposed from $r_{\alpha\beta}^s$ (1.2 $\sigma_{\alpha\beta}$) to $r_{\alpha\beta}^c$, roughly in between the first neighbor shell and second neighbor shell. The larger the energy penalty, the more brittle the model glass. Here, the relative barrier height ε_B is set as 0.4, which corresponds to a very brittle glass in its bulk form. The reference time scale can be defined as $t_0 = \sigma_{LL} \sqrt{m_0/\varepsilon_{LL}}$; therefore, all physical quantities can be expressed in SI units following a previous report mapping to a

binary metallic glass $Ni_{50}Nb_{50}^{35}$: $\sigma_{LL} \approx 0.27$ nm, $m_0 \approx 46$ amu, $\varepsilon_{LL} \approx 0.151$ eV, $t_0 \approx 0.5$ ps. This potential has been previously utilized in investigating the intrinsic ductility of amorphous solids,³⁶ the low cycle fatigue of metallic nanowires,³⁷ the crack initiation of metallic glasses under nanoindentation,³⁸ fracture energy and Poisson's ratio correlation in metallic systems,³⁹ designing workhardenable nanocomposite, 40 as well as the dynamic and mechanic properties of polymeric materials with simple modification.⁴

B. Compression test setup

The compression test setup for an as-quenched nanoparticle (AQ-NP) is as follows. A cubic liquid sample, with a dimension of 10.2 nm and a number density of 60.2 atoms/nm³, was first equilibrated at 2100 K and then quenched isochorically to 28 K in 0.5 ns.

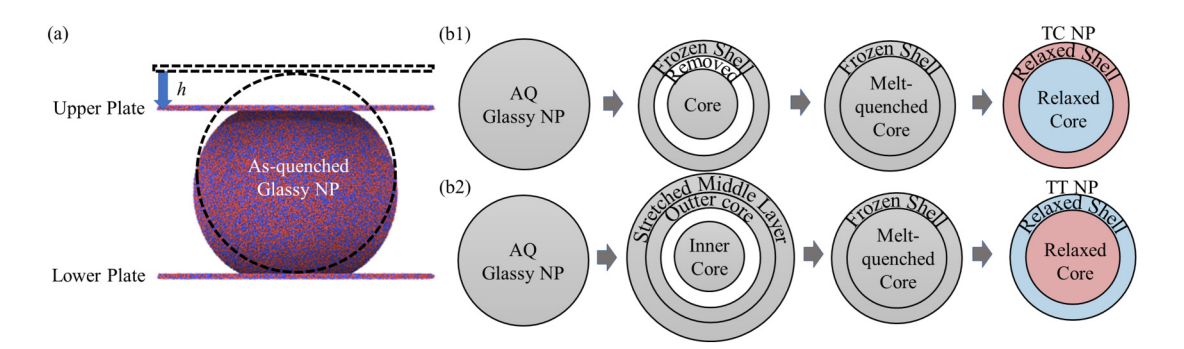


FIG. 1. (a) Schematic of the simulation system for nanoparticle compression. The displacement of the upper plate is h. (b1) Schematic of preparing a tempered glassy nanoparticle with compressive surface stress (TC-NP) using an as-quenched nanoparticle (AQ-NP). (b2) Schematic of preparing a tempered glassy nanoparticle with tensile surface stress (TT-NP) also from an AQ-NP.

The density was chosen such that the final glassy sample is nearly stress free. The bulk glassy sample was further relaxed for 0.4 ns at 28 K to relieve any residual stress. Next, the bulk glassy sample was replicated to carve out a spherical nanoparticle (radius varying from 13.5 to 54 nm) and two rigid plates as shown in Fig. 1(a). As the stress field for a compressed nanoparticle is inhomogeneous, the replication of bulk glass will not lead to artificial periodicity in the mechanical response. The thickness of the rigid plate is 0.54 nm. There are no periodic boundary conditions applied such that the compression of nanoparticles is completely isolated. For simplicity, both the plate and the nanoparticles are made of the same aforementioned binary modified Lennard-Jones glass.

The compression test on the glassy nanoparticles was carried out by moving the upper rigid plate downward with a speed of 27 m/s and keeping the lower rigid plate stationary. The progression of the compression is characterized by the displacement of the upper plate (h) and normalized by the radius of the nanoparticle (r). Note that as the lower plate does not move, the actual displacement of the nanoparticle center relative to either plate (equivalent to indentation depth) is only half of h. A temperature of 28 K is maintained by coupling a Nose–Hoover thermostat 42,43 during compression. This very low temperature is used here to ensure that the model glass is brittle and the size-dependent BTD is accessible in MD simulations.

C. Sample preparation for tempered nanoparticle

In addition to the as-quenched sample, two different types of tempered glassy nanoparticles were prepared as follows [Fig. 1(b)]. To prepare a glassy nanoparticle with a compressive surface layer (TC-NP), a middle shell from the AQ-NP was removed. The core region was then subjected to the same melt-quench procedure described above, while being contained by a frozen outer shell with a thickness of 2.7 nm. Due to the removed middle shell, the final glass density is 53.8 atoms/nm³ and, thus, exhibits tensile stress. Finally, both the shell and the core were relaxed at 28 K for 0.5 ns to reach mechanical equilibrium. The core pulls the shell inward such that a compressive stress was developed in the surface layer. Similarly, to prepare a glassy nanoparticle with a tensile surface layer (TT-NP), a middle shell from the AQ-NP was stretched in all

directions to become the outer layer (thus, lower density) with a thickness of 1.35 nm. The whole nanoparticle then shrinks such that the liquid (both outer core and inner core) inside the stretched shell retains the same density as the original AQ samples. The core region was then subjected to the same melt-quenching procedure with the stretched shell frozen. Finally, both the shell and the core were relaxed at 28 K. In this way, glassy nanoparticles with either tensile or compressive surface stress with an intimate core–shell interface, guaranteed by the melt-quench process, can be obtained.

III. RESULTS AND DISCUSSIONS

A. Normalized load-displacement curve

Figure 2(a) shows the load F_y (averaged over both plates, $\frac{7}{2}$) then normalized by r^2 , r is the NP radius) vs the displacement h (normalized by r) curve. F_y/r^2 represents the compressive stress, while h/r represents the compressive strain. Thus, the normalized load–displacement curve is analogous to the stress–strain curve in a uniaxial compression test, albeit with non-uniform stress distribution. According to the Hertzian solution (h/2 is equivalent to the indentation depth),

$$F_{y} = \frac{4}{3} E^{*} r^{\frac{1}{2}} \left(\frac{h}{2}\right)^{\frac{3}{2}}.$$
 (2)

Thus, the normalized load-displacement relation is

$$\frac{F_y}{r^2} = \frac{\sqrt{2}}{3} E^* \left(\frac{h}{r}\right)^{\frac{3}{2}},\tag{3}$$

where r is the radius of the nanoparticle, h is the displacement of the upper plate, and E^* is the reduced modulus for the nanoparticle–plate contact,

$$\frac{1}{E^*} = \frac{1 - v_{NP}^2}{E_{NP}} + \frac{1 - v_{Plate}^2}{E_{Plate}}.$$
 (4)

The model glass has Young's modulus of 100.3 GPa and Poisson's ratio of 0.25, which were obtained by a separate uniaxial

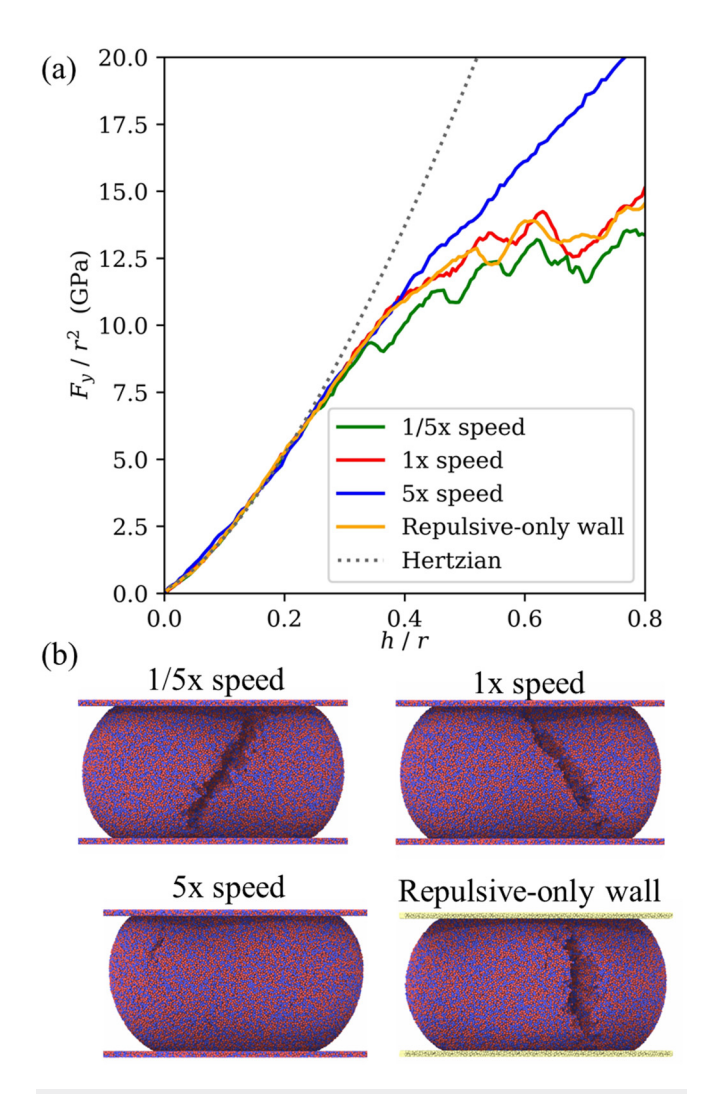


FIG. 2. (a) Normalized load–displacement curves for a nanoparticle with 13.5 nm radius under three different loading speeds of 5.4 (1/5x speed, green), 27 (1x speed, red), and 135 m/s (5x speed, blue). The normalized load–displacement for compression using the repulsion-only plate is the orange line. The Hertzian elastic solution is the black dotted line. (b) Deformation morphologies of AQ-NP compressed under four different conditions at *h/r* of 0.8.

compression test of the same glassy sample. The plate is rigid, thus, has infinite Young's modulus. Therefore, the reduced modulus E^* is calculated to be 106.7 GPa. Figure 2(a) shows that all normalized load–displacement curves from MD simulations show excellent agreement with the Hertzian solution of Eq. (3) up to around h/r of 0.25, after which plastic deformation and/or fracture may occur.

B. Effect of loading rate and nanoparticle-plate interaction

It is important to examine the effect of the compression rate, as shown in Fig. 2. Here, 1x speed denotes the default upper plate

speed of 27 m/s. One can see that compression using one-fifth of the original speed leads to a slightly earlier initial drop in the normalized load–displacement curve, and a generally softer response from the glassy nanoparticle, yet the almost identical appearance of the fracture surface as shown in Fig. 2(b). However, for the compression test with five times the original speed, the mechanical response is much stronger with almost no discernable stress drop, which indicates considerably reduced plastic events. There is also no visible surface crack up to h/r = 0.8 for high-speed compression. From the results presented in Fig. 2, we concluded that the original speed (27 m/s) is slow enough to produce qualitative very similar results to the much slower compression rate, which will be used throughout this work.

We also examined the effect of the nanoparticle–plate interaction. The original nanoparticle–plate interaction is essentially the same as in the binary glass. Due to the "bump" present in the pairwise interaction [Eq. (1)], the initial contact is purely repulsive. As the plate is pushed further into the glassy particle, the interaction could be either attractive or repulsive depending on nanoparticle–plate separation. For the repulsive-only plate, the cutoffs of all interactions across the nanoparticle and plate are set as $r_{\alpha\beta}^c = 2^{\frac{1}{6}} \sigma_{\alpha\beta}$ (the potential minimum) with zero barrier height such that all types of interactions become purely repulsive. It can be seen from the normalized load–displacement curve and the surface morphology of the nanoparticle (as in Fig. 2) that the original plate (with adhesion) and the repulsion-only plate behave quite similarly. For simplicity, the original plate with adhesion was used throughout this work.

C. Effect of nanoparticle size

To investigate how the size of the nanoparticle affects the deformation behavior under compression, we have prepared AQ glassy nanoparticles with radius ranging from 13.5 to 54 nm. Figure 3 shows the deformation morphologies for *h/r* ranging from

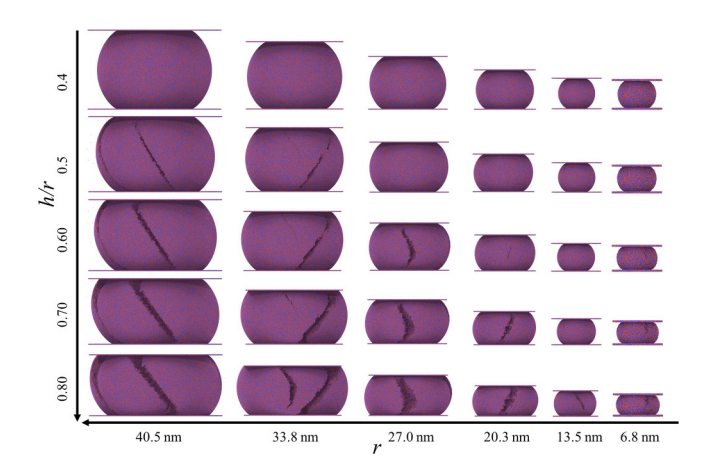


FIG. 3. Deformation morphologies of AQ-NPs with different radii as labeled with increasing *hlr* from top to bottom. All images are consistent in the spatial scale except for the smallest nanoparticle (magnified twice to show details).

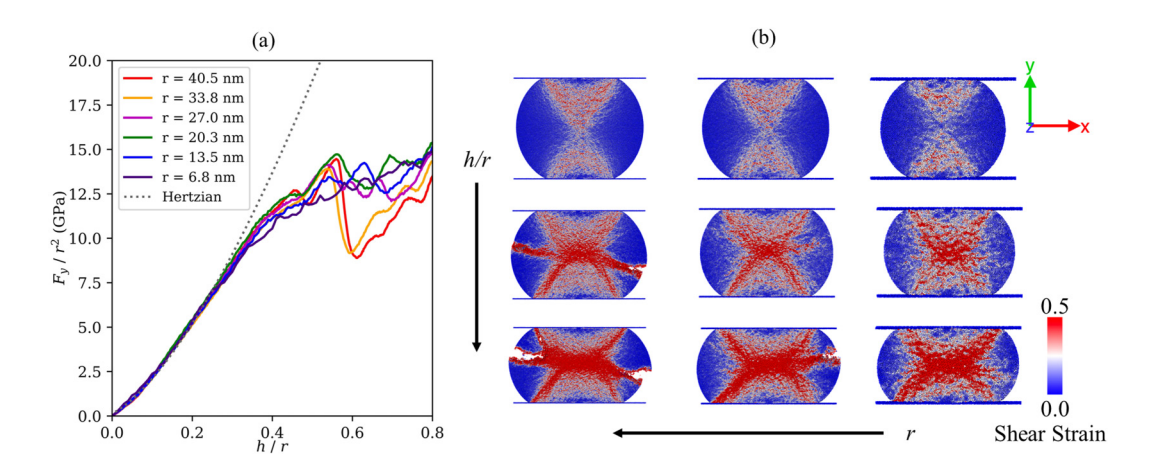


FIG. 4. (a) Normalized load-displacement curves for the AQ-NP with different radii as shown in Fig. 3. (b) Deformation morphology shown on the cross sections through the AQ-NP center during compression for three particle radii of 40.5, 27, and 13.5 nm, and at h/r of 0.4, 0.6, and 0.8. The atoms are colored according to the accumulative shear strain in reference to the initial uncompressed nanoparticle.

0.4 to 0.8. As the nanoparticle size becomes smaller, the fracture commences at a higher h/r. For the two smallest nanoparticles, surface fracture is hardly visible until about h/r of 0.8. Figure 4(a) shows the normalized load-displacement curves for nanoparticles with different radii. Deviation from the Hertzian solution appears around h/r of 0.25 regardless of the nanoparticle size. For small nanoparticles, the serration in the normalized load-displacement curve is minor. However, dramatic drops in the normalized loaddisplacement occur for large nanoparticles, indicating large shear banding or fracture events. Such size-dependency is consistent with the deformation morphology shown in Fig. 3.

Figure 4(b) shows the accumulative local shear deformation distribution for a middle slice of the nanoparticle during compression. The shear strain is calculated using OVITO following earlier formulations.44,4 ¹⁵ Regardless of the nanoparticle size, deformation starts with shear band formation axially symmetric around the loading direction. The shear bands seem to generally cross at the center of the nanoparticle as well. This very initial deformation of the nanoparticle under flat-punch compression is somewhat similar to uniaxial compression albeit with elevated stress near the contact, as well as the non-contacting buttressing materials around the middle core. The buttressing region would later develop tensile stress [as shown in Fig. 6] despite under overwhelming compression from the flat punch, which eventually forms cracks. In addition, the shear band direction is around 34° (off the loading direction), which is likely due to the fact that the yield criterion is normal-stress dependent. 46 For large nanoparticles, crack formation seems to be following the shear band, which indicates that cavitation is likely to be shear-assisted.³⁸ For small nanoparticles, the plastic flow appears to continue from the initial shear bands without creating cracks.

D. Effect of surface stress for tempered nanoparticles

Tempered glass has been widely used in everyday life, yet how the compressive surface layer affects deformation at the atomic

level is not well understood. Here, using the compression of tempered nanoparticles, we could examine how the surface stress state affects deformation on otherwise identical nanoparticles. We have also included tempered nanoparticle with tensile surface stress for comparison purposes. Figure 5(a) shows that the strength of the TC-NP (with compressive surface stress) is considerably stronger than both the AQ-NP (no surface stress) and TT-NP (with tensile Signature) surface stress), with the latter two behaving similarly. As shown in graph in the TC NP. In addition, we have graph. while no cracks appear in the TC-NP. In addition, we have examined how the surface stress state affects notch sensitivity by introducing a disk-shaped crack inside the nanoparticles as shown in 2 Fig. 5(a), inset. Although all three nanoparticles suffer noticeable reduction in strength, the surface morphology differs considerably. The surface crack grows significantly in the TT-NP under compression, while it is almost invisible in the TC-NP under the same loading condition. The AQ-NP behaves somewhat in the middle.

The stress distribution of the middle slice of pristine AQ-NP, TC-NP, and TT-NP during compression can be seen from Fig. 6. For the AQ-NP, there is no initial stress distribution. Under compression, only compressive stress initially develops, and it is concentrated near the contact. Finally, tensile stress develops near the surface in the buttressing region (to a lesser extent, at the particle center), which then leads to surface crack formation. For the TC-NP, there is an initial compressive stress in the surface region from our sample preparation, which leads to delayed tensile stress development in the buttressing regions, thus delayed surface crack formation. It is also interesting to note that the initial stress in the core region of the TC-NP is slightly tensile to maintain mechanical equilibrium, which becomes compressive as the loading proceeds. For the TT-NP, the initial stress distribution is a compressive core with a tensile surface layer, which is exactly opposite to the TC-NP. The core region of the TT-NP, which is similar to the AQ-NP, turns from compressive to slightly tensile in the intermediate compression stage, before becoming overwhelmingly compressive in the later stage.

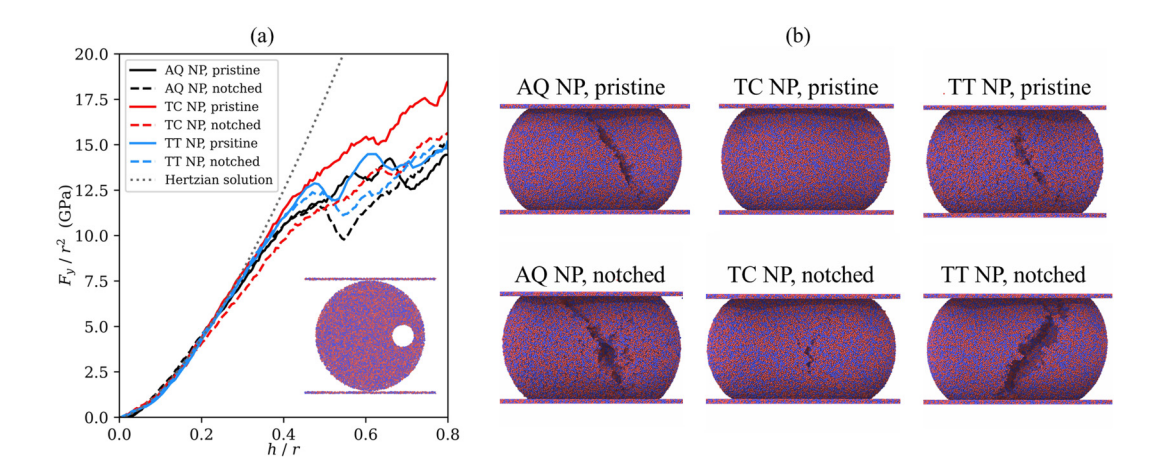


FIG. 5. (a) Normalized load-displacement curves for AQ-NP, TC-NP, and TT-NP with or without a notch. The radius is about 13.5 nm. The inset shows the diagram of the notch. The notch is disk-shaped with a thickness of 2.7 nm and a radius of 2.7 nm. The distance between the right edge of the notch and the closest surface is also 2.7 nm. (b) Deformation morphologies of the three NPs under compression at the same h/r of 0.8.

To further investigate the differences in mechanical responses of nanoparticles as a result of the initial stress distribution, deformation events in terms of either shear or local crack formation are analyzed at the atomic level as shown in Fig. 7. The shear events are characterized by the number of atoms experiencing local instantaneous shear strain higher than 10% compared to the preceding system snapshot (the difference is 0.05 in terms of h/r). The internal crack formation is tracked by counting the atoms in the core region (excluding 2.7 nm thickness of the surface) with less than 6 nearest neighbor atoms (12 is roughly the average). The identification of nearest neighbor pairs is based on cutoff distances of 0.27, 0.22, and 0.25 nm for the L-L, S-S, and L-S pairs, respectively. For the AQ-NP, shear deformation occurs around h/r of 0.25, which is similar to the deviation from the elastic solution as shown in the normalized load-displacement curve in Fig. 2. Only after a significant amount of shear banding, internal fracture occurs around h/r of 0.62, which corresponds to the largest dip in the

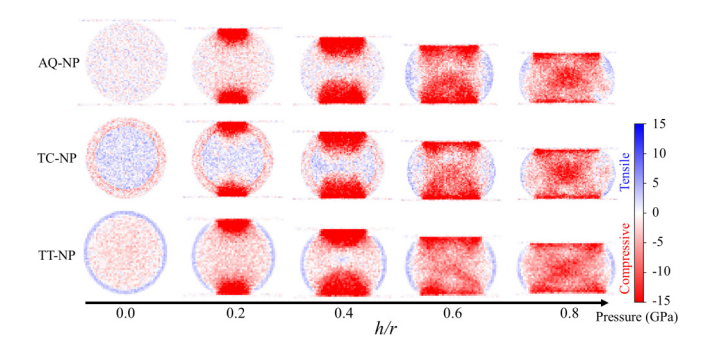


FIG. 6. Local pressure distribution in AQ-NP, TC-NP, and TT-NP with a radius of 13.5 nm during compression with increasing h/r (0.2 increments). The local pressure is coarse-grained using the atomic stress tensor over a grid size of 0.32 by 0.32 by 2.7 nm.

normalized load-displacement curve. This observation also justifies our structural criterion in terms of nearest neighbor atoms to identify the internal crack. For the TC-NP, shear events occur much earlier than the AQ-NP, probably due to the initial inhomogeneous stress distribution. Shear events, instead of fracture, seem to cause the first dip in the normalized load-displacement curve. Internal crack formation only occurs around h/r of 0.70, causing the second dip in the normalized load-displacement curve. For the TT-NP, shear events are more prevalent than the TC-NP, and the internal fracture occurs slightly earlier with more internal surface formed. fracture occurs slightly earlier with more internal surface formed. Thus, the tensile surface promotes both shear and fracture as in the TT-NP, while the compressive surface promotes shear and inhibits fracture as in the TC-NP. Our MD results show that although the 3 fracture is delayed in the TC-NP, irreversible damage in terms of shear occurs much earlier than in the AQ-NP, which could compromise the mechanical performance for instance under cyclic loading.

E. Critical size of nanoparticle for the BTD transition

We have presented so far the size-dependent mechanical response of glassy nanoparticles in Fig. 3, the stress distribution in Fig. 6, and shear/fracture competition in Fig. 7. To further quantify the size-dependent deformation of the nanoparticle in compression, we have developed a simple Griffith's type fracture model as detailed below.

Similar to Griffith's energy consideration for brittle fracture, one can calculate both the elastic energy stored in the nanoparticle and the energy penalty for creating new surfaces upon fracture. Let us assume perfect elastic deformation up to h_{max} of compression, which is equivalent to both plates, each displaces $h_{max}/2$. Therefore, the maximum elastic energy stored can be calculated from the work done by both plates using Eq. (2),

$$\Delta E_{elastic} = 2 \int_{0}^{\frac{h_{max}}{2}} F_{y} dy = \frac{16}{15} E^{*} r^{\frac{1}{2}} \left(\frac{h_{max}}{2} \right)^{\frac{5}{2}}.$$
 (5)

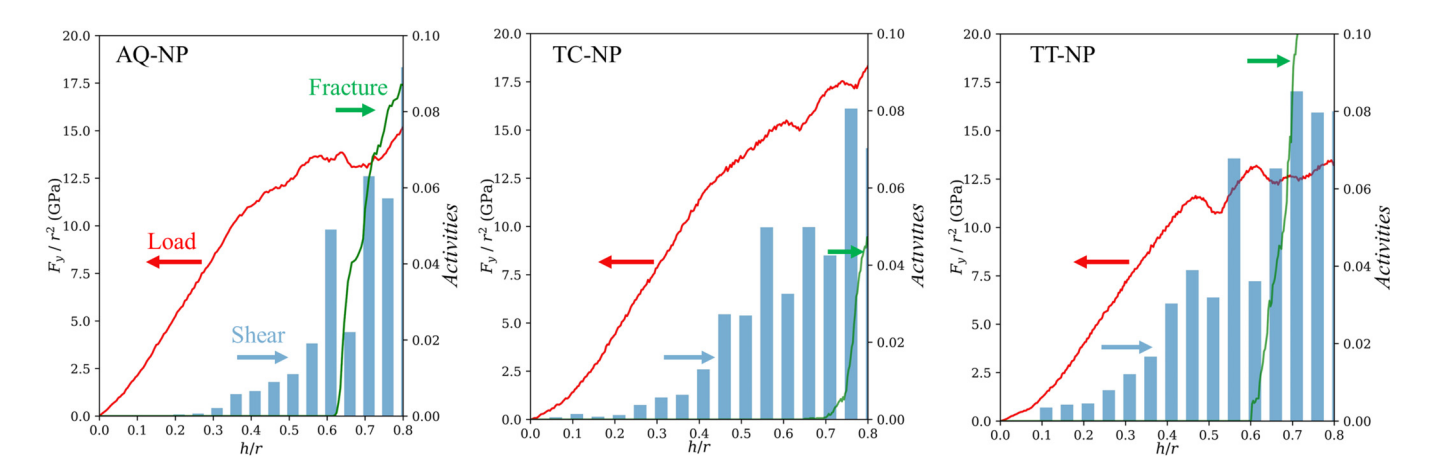


FIG. 7. Normalized load (red line), shear activities (blue bar), and fracture activities (green line) as a function of *h/r* for AQ-NP, TC-NP, and TT-NP. Thus, the alternative vertical axis "activities" represent both the shear activities and fracture activities. The blue bar represents instantaneous shear activities, which is the fraction of atoms experiencing local shear strain larger than 10%. The instantaneous shear strain is calculated with reference to the system's previous snapshot with a D*h/r* of 0.05. The green line represents the fracture activities, which is the fraction of non-surface atoms with fewer than six nearest neighbors. This fraction for fracture activities is magnified by 200 for clarity.

Based on the normalized load–displacement in Fig. 4, we can estimate h_{max}/r to be roughly twice the elastic limit in uniaxial compression (ϵ_{el} is around 0.11). Thus,

$$\Delta E_{elastic} = \frac{16}{15} E^{\dagger} r^3 \epsilon_{el}^{\frac{5}{2}}.$$
 (6)

To estimate the new surface creation during fracture, one can consider a simple cleavage at the center (Γ is the surface energy),

$$\Delta E_{fracture} = 2\pi r^2 \Gamma. \tag{7}$$

As the elastic energy increases with a higher exponent than the fracture energy, a critical radius can be derived when the elastic energy stored equals that of the energy penalty for surface creation,

$$r_{critical} = \frac{15\pi\Gamma}{8E^*\epsilon_{\rho l}^{\frac{5}{2}}}.$$
 (8)

The surface energy can be calculated by creating two surfaces from bulk glass and measuring the potential energy increase (without any relaxation) per surface area created. The unrelaxed surface energy for this model glass is measured to be around 2.3 J/m², and together with the reduced modulus of 106.7 GPa, the critical radius for BTD transition is calculated to be ~30 nm. Therefore, nanoparticles with radius lower than 30 nm do not possess a sufficient amount of elastic energy (when compressed to the point of yield) to drive the formation of ideal cleavage, and vice versa. It should be noted that Griffith's energy argument is only a necessary condition; thus, Eq. (8) serves as a crude estimate for the BTD transition for brittle nanoparticles.

As an example, one can estimate the critical radius for silica nanoparticle (surface energy estimated to be half the fracture energy of ~4 J/m^{2,47} Young's modulus of 70 GPa, Poisson's ratio of 0.15, and compressive yield stress of 7 GPa;⁴⁸ thus, elastic strain limit of 0.10) to be about 52 nm. On a last note, the above model considers the BTD transition in an ideal spherical nanoparticle under compression, which is different from Kendall's earlier model⁵ that considered the BTD transition in a wedged-shaped plate-like particle, and more importantly, with a crack inside.

IV. CONCLUSIONS

In this study, we conducted a systematic investigation of glassy nanoparticles under compression using flat punches. Our findings show that the elastic deformation of the nanoparticles can be accurately described by the Hertzian solution. Subsequently, extensive shear banding occurs, followed by the formation of cracks around the tensile buttressing region of the nanoparticles. Importantly, we found that the formation of cracks is highly dependent on the nanoparticle size, and we derived a critical size for the brittle-to-ductile transition analytically. Furthermore, we examined the deformation behavior of tempered nanoparticles with surface stress. We observed that nanoparticles with compressive surface stress exhibited enhanced strength and reduced defect sensitivity, which can be attributed to the promotion of shear and the delayed emergence of the tensile region. In contrast, nanoparticles with tensile surface stress had enhanced defect sensitivity, mainly due to the promotion of the tensile region, even with increased shear activities. The insights gained from our study on the deformation behavior of single nanoparticles can serve as a foundation for understanding the behavior of more complex nanoparticles with compositional or stress gradients, under both shear and compression, in the presence of lubricants or smaller debris particles, as well as multiple nanoparticles interacting with each other. We believe that compression tests of nanoparticles, being the "inverse nanoindentation," could serve as a standard

protocol for measuring material mechanical properties, particularly plasticity and fracture in confined spaces.

ACKNOWLEDGMENTS

This work was supported by the National Science Foundation under Grant Nos. DMR-2015557 and DMR-1936368. We would like to thank Dr. Catalin Picu, Dr. Gyorgy Korniss, Dr. Gwo Ching Wang, and Dr. Shengbai Zhang from Rensselaer Polytechnic Institute for stimulating discussions. The simulations were carried out on supercomputers in the Center for Computational Innovations (CCI) at Rensselaer.

AUTHOR DECLARATIONS

Conflict of Interest

The authors have no conflicts to disclose.

Author Contributions

Marx Akl: Data curation (lead); Formal analysis (lead); Investigation (lead); Visualization (lead); Writing – original draft (equal); Writing – review & editing (equal). Liping Huang: Conceptualization (equal); Investigation (equal); Writing – original draft (equal); Writing – review & editing (equal). Yunfeng Shi: Conceptualization (equal); Formal analysis (equal); Investigation (equal); Project administration (equal); Supervision (lead); Writing – original draft (equal); Writing – review & editing (equal).

DATA AVAILABILITY

The data that support the findings of this study are available from the corresponding author upon reasonable request.

REFERENCES

- ¹V. L. Popov, "Is tribology approaching its golden age? Grand challenges in engineering education and tribological research," Front Mech. Eng. 4, 16 (2018).
- ²I. U. Vakarelski and K. Higashitani, "Single-nanoparticle-terminated tips for scanning probe microscopy," <u>Langmuir</u> 22(7), 2931–2934 (2006).
- ³J. L. Mead, W. Klauser, F. von Kleist-Retzow, and S. Fatikow, "Advances in assembled micro- and nanoscale mechanical contact probes," Front Mech. Eng. 8, 983334 (2022).
- ⁴N. Baig, I. Kammakakam, and W. Falath, "Nanomaterials: A review of synthesis methods, properties, recent progress, and challenges," Mater. Adv. 2(6), 1821–1871 (2021).
- ⁵K. Kendall, "The impossibility of comminuting small particles by compression," Nature 272(5655), 710–711 (1978).
- ⁶C.-N. Yuan, Y.-F. Li, Y.-J. Sheng, and H.-K. Tsao, "Dry nanogranular materials," Appl. Phys. Lett. 98(14), 144102 (2011).
- ⁷J. Akedo, "Room temperature impact consolidation (RTIC) of fine ceramic powder by aerosol deposition method and applications to microdevices," J. Therm. Spray Technol. 17(2), 181–198 (2008).
- ⁸J. Akedo, "Room temperature impact consolidation and application to ceramic coatings: Aerosol deposition method," J. Ceram. Soc. Jpn. **128**(3), 101–116 (2020).
- ⁹T. Burgess and M. Ferry, "Nanoindentation of metallic glasses," Mater. Today 12(1), 24–32 (2009).
- ¹⁰G. Dehm, B. N. Jaya, R. Raghavan, and C. Kirchlechner, "Overview on microand nanomechanical testing: New insights in interface plasticity and fracture at small length scales," Acta Mater. 142, 248–282 (2018).

- ¹¹F. Yang and J. C. M. Li, Micro and Nano Mechanical Testing of Materials and Devices (Springer US, Boston, MA, 2008).
- ¹²C. T. Pan, T. T. Wu, J. K. Tseng, C. Y. Su, W. J. Wang, and J. C. Huang, "Mechanical behavior of metallic glasses Mg-Cu-Y using nano-indentation," Microsyst. Technol. 16(4), 585–593 (2010).
- ¹³J. R. Greer, W. C. Oliver, and W. D. Nix, "Size dependence of mechanical properties of gold at the micron scale in the absence of strain gradients," Acta Mater. 53(6), 1821–1830 (2005).
- ¹⁴Y. Hu, L. Shu, Q. Yang, W. Guo, P. K. Liaw, K. A. Dahmen, and J.-M. Zuo, "Dislocation avalanche mechanism in slowly compressed high entropy alloy nanopillars," Commun. Phys. 1(1), 1–8 (2018).
- ¹⁵D. Jang and J. R. Greer, "Transition from a strong-yet-brittle to a stronger-and-ductile state by size reduction of metallic glasses," Nat. Mater. 9(3), 215–219 (2010).
- ¹⁶W. Gonçalves, J. Amodeo, J. Morthomas, P. Chantrenne, M. Perez, G. Foray, and C. L. Martin, "Nanocompression of secondary particles of silica aerogel," Scr. Mater. 157, 157–161 (2018).
- ¹⁷I. M. Padilla Espinosa, S. Azadehranjbar, R. Ding, A. J. Baker, T. D. B. Jacobs, and A. Martini, "Platinum nanoparticle compression: Combining *in situ* TEM and atomistic modeling," Appl. Phys. Lett. **120**(1), 013101 (2022).
- ¹⁸I. Z. Jenei, F. Dassenoy, T. Epicier, A. Khajeh, A. Martini, D. Uy, H. Ghaednia, and A. Gangopadhyay, "Mechanical characterization of diesel soot nanoparticles: *In situ* compression in a transmission electron microscope and simulations," Nanotechnology **29**(8), 085703 (2018).
- 19S. Kuroyanagi, K. Shinoda, A. Yumoto, and J. Akedo, "Size-dependent quasi brittle-ductile transition of single crystalline alpha-alumina particles during microcompression tests," Acta Mater. 195, 588–596 (2020).
- ²⁰A. Sharma, O. Mendelsohn, A. Bisht, J. Michler, R. K. Koju, Y. Mishin, and E. Rabkin, "Solid-solution and precipitation softening effects in defect-free faceted nickel-iron nanoparticles," Acta Mater. 243, 118527 (2023).
- 21 D. Veysset, J.-H. Lee, M. Hassani, S. E. Kooi, E. L. Thomas, and K. A. Nelson, "High-velocity micro-projectile impact testing," Appl. Phys. Rev. 8(1), 011319
- ²²I. Dowding, M. Hassani, Y. Sun, D. Veysset, K. A. Nelson, and C. A. Schuh, "Particle size effects in metallic microparticle impact-bonding," Acta Materialia 194, 4048 (2020).
- 23Y. Sun, D. Veysset, K. A. Nelson, and C. A. Schuh, "The Transition From Rebound to Bonding in High-Velocity Metallic Microparticle Impacts: Jetting-Associated Power-Law Divergence," J. Appl. Mech. 87, 091002, (2020).
- ²⁴J. Amodeo and L. Pizzagalli, "Modeling the mechanical properties of nanoparticles: A review," C. R.. Phys. 22(S3), 1–32 (2021).
- ²⁵I. M. Padilla Espinosa, T. D. B. Jacobs, and A. Martini, "Atomistic simulations of the elastic compression of platinum nanoparticles," Nanoscale Res. Lett. 17(1), 96 (2022).
- ²⁶I. Z. Jenei, F. Dassenoy, T. Epicier, A. Khajeh, A. Martini, D. Uy, H. Ghaednia, and A. Gangopadhyay, "Mechanical response of gasoline soot nanoparticles under compression: An in situ TEM study," Tribology International 131, 446–453 (2019).
- ²⁷P. Valentini, W. W. Gerberich, and T. Dumitrică, "Phase-Transition plasticity response in uniaxially compressed silicon nanospheres," Phys. Rev. Lett. 99(17), 175701 (2007).
- 28D. Kilymis, C. Gérard, J. Amodeo, U. V. Waghmare, and L. Pizzagalli, "Uniaxial compression of silicon nanoparticles: An atomistic study on the shape and size effects," Acta Mater. 158, 155–166 (2018).
- ²⁹W. D. Callister Jr and D. G. Rethwisch, Fundamentals of Materials Science and Engineering: An Integrated Approach (John Wiley & Sons, 2020).
- ³⁰R. Gardon, in *Glass Science and Technology*, edited by D. R. Uhlmann and N. J. Kreidl (Elsevier, 1980), pp. 145–216.
- ³¹T. O. Olugbade and J. Lu, "Literature review on the mechanical properties of materials after surface mechanical attrition treatment (SMAT)," Nano Mater. Sci. 2(1), 3–31 (2020).
- 32S. Ghosh, N. Bibhanshu, S. Suwas, and K. Chatterjee, "Surface mechanical attrition treatment of additively manufactured 316L stainless steel yields gradient nanostructure with superior strength and ductility," Mater. Sci. Eng. A 820, 141540 (2021).

- 33S. Plimpton, "Fast parallel algorithms for short-range molecular dynamics," J. Comput. Phys. 117(1), 1–19 (1995).
- ³⁴Y. Shi, "Creating atomic models of brittle glasses for in silico mechanical tests," Int. J. Appl. Glass Sci. 7(4), 464–473 (2016).
- 35Y. Shi and M. L. Falk, "Structural transformation and localization during simulated nanoindentation of a noncrystalline metal film," Appl. Phys. Lett. 86(1), 011914 (2005)
- ³⁶Y. Shi, J. Luo, F. Yuan, and L. Huang, "Intrinsic ductility of glassy solids," J. Appl. Phys. 115(4), 043528 (2014).
- ³⁷J. Luo, K. Dahmen, P. K. Liaw, and Y. Shi, "Low-cycle fatigue of metallic glass nanowires," Acta Mater. 87, 225–232 (2015).
- ³⁸Y. Yang, J. Luo, L. Huang, G. Hu, K. D. Vargheese, Y. Shi, and J. C. Mauro, "Crack initiation in metallic glasses under nanoindentation," *Acta Mater.* 115, 413–422 (2016).
- 413–422 (2016).

 ³⁹B. Deng and Y. Shi, "On measuring the fracture energy of model metallic glasses," J. Appl. Phys. **124**(3), 035101 (2018).
- glasses," J. Appl. Phys. 124(3), 035101 (2018).

 40Y. Zhang, H. Zhao, B. Deng, S. Basu, L. Huang, and Y. Shi, "Design ductile and work-hardenable composites with all brittle constituents," Acta Mater. 208, 116770 (2021).

- ⁴¹B. Deng, L. Huang, and Y. Shi, "Solvent effect on the diffusion of unentangled linear polymer melts," Langmuir 33(42), 11845–11850 (2017).
- ⁴²S. Nosé, "A unified formulation of the constant temperature molecular dynamics methods," J. Chem. Phys. **81**(1), 511–519 (1984).
- ⁴³W. G. Hoover, "Canonical dynamics: Equilibrium phase-space distributions," Phys. Rev. A 31(3), 1695–1697 (1985).
- ⁴⁴F. Shimizu, S. Ogata, and J. Li, "Theory of shear banding in metallic glasses and molecular dynamics calculations," Mater. Trans. **48**(11), 2923–2927 (2007).
- ⁴⁵M. L. Falk and J. S. Langer, "Dynamics of viscoplastic deformation in amorphous solids," Phys. Rev. E 57(6), 7192–7205 (1998).
 ⁴⁶M. Vargonen, L. Huang, and Y. Shi, "Evaluating mohr–Coulomb yield crite-
- ⁴⁶M. Vargonen, L. Huang, and Y. Shi, "Evaluating mohr–Coulomb yield criterion for plastic flow in model metallic glasses," J. Non-Cryst. Solids 358(24), 3488–3494 (2012).
- 47J. P. Lucas, N. R. Moody, S. L. Robinson, J. Hanrock, and R. Q. Hwang, "Determining fracture toughness of vitreous silica glass," Scr. Metall. Mater. 32(5), 743–748 (1995).
- ⁴⁸G. Kermouche, G. Guillonneau, J. Michler, J. Teisseire, and E. Barthel, "Perfectly plastic flow in silica glass," Acta Mater. 114, 146–153 (2016).